Ocean Engineering 234 (2021) 109277

Contents lists available at ScienceDirect

Ocean Engineering

journal homepage: www.elsevier.com/locate/oceaneng

Towing-tank measurement of unsteady wave elevation around two ships in head sea condition and comparison with computational results

Jaehoon Lee [a], Yonghwan Kim [b,*]

[a] Korea Research Institute of Ships & Ocean Engineering (KRISO), Daejeon, Republic of Korea
[b] Seoul National University, Seoul, Republic of Korea

ARTICLE INFO

Keywords:
Unsteady ship waves
Waves around ships
Wave measurement
Seakeeping
EFD vs. CFD
WISH

ABSTRACT

Many studies on ship wave elevation measurement have been performed focusing on steady waves in calm water and unsteady wave-cut analysis near ships, and a reliable experimental database of unsteady wave elevation with incident waves is not enough for the validation of numerical computations. In this study, a non-contact scheme for capturing the instantaneous free surface near two ships is adopted to avoid any disturbance caused by measuring equipment. The applicability of the newly established unsteady measurement technique is examined during a standard seakeeping test with various wave amplitudes. Heave and pitch motions are set free, while the soft spring system is used for surge motion. The instantaneous free surface elevation is obtained on equally spaced positions. The mean value and higher harmonic components of measured wave elevation clearly show nonlinear characteristics for various incident wave amplitudes. Snapshots at several time instants and the magnitude of the first harmonic components of unsteady wave elevation are compared with those of numerical computations based on a Rankine panel method. The overall trend shows fair correspondence, whereas the detailed local flows are somewhat different because of the nonlinearity of waves.

1. Introduction

Based on the firm foundation of ship motion theory, linear and nonlinear motion analyses show reasonable results for the general hull forms with moderate speed. However, added resistance shows significant discrepancies among the different methodologies. To overcome this difficulty, analysis methods have been examined to improve their accuracy. During this process, reliable reference data is needed; however, for nonlinear phenomena, few exact solutions may exist within the satisfactory level. Therefore, experimental data with uncertainty analysis is urgently needed for validation purposes. Among the various parameters, free surface elevation around the body in waves is a fascinating source. Also known as the wave pattern or Kochin function, free surface elevation characteristics are related to steady and unsteady hull pressure and added resistance.

Various investigations have been conducted based on wave analysis in calm water. Chronicles are well organized in Wehausen (1973) and recently Kompe (2014) regarding analytical, numerical, and experimental approaches. Janson and Spinney, 2004 discussed various wave analysis methods, and Kim et al. (2001) show wave patterns near a benchmark hull with KRISO Container Ship (KCS) and KRISO Very Large Crude Carrier 2 (KVLCC2). Olivieri et al. (2007) analyzed the breaking wave phenomena around a hull bow and shoulder using a servo-needle-type wave probe.

These wave analyses in calm and deep water are performed because of the increased reliability compared with direct pressure and force measurements. However, analysis of unsteady free surfaces needs to overcome higher difficulty because of the irregularity of the flow, including breaking waves, and difficulty of conducting repeat tests to acquire sufficient data. The few existing experimental studies related to unsteady waves are categorized into image-processing methods and contact-type wave probe methods. Shigeru et al. (1998) adopted a light-source method for image capture and post-processing with a Series 60 (Cb = 0.6) hull in regular waves in motion-free conditions. Iwashita et al. (1990, 2011) applied the so-called "multi-fold method (Okhusu, 1980)", which uses multiple one-row-earth-fixed wave probes to reconstruct the 3D wave amplitude function, i.e. Kochin function for a modified Wigley hull. Kashiwagi (2013) reported analytical approaches for evaluating added resistance based on the measurement data of Iwashita et al. (2011). Gui et al. (2001, 2002) conducted experiments for

* Corresponding author. Department of Naval Architecture and Ocean Engineering, Seoul National University, 1 Gwanak-ro, Gwanak-gu, Seoul, 08826, Republic of Korea.
E-mail addresses: j.lee@kriso.re.kr (J. Lee), yhwankim@snu.ac.kr (Y. Kim).

https://doi.org/10.1016/j.oceaneng.2021.109277
Received 8 January 2021; Received in revised form 30 May 2021; Accepted 31 May 2021
Available online 10 June 2021

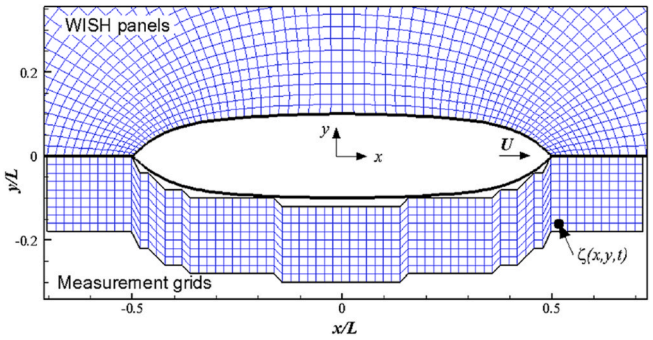

Fig. 1. Coordinate system, measurement grid and computational panels.

a fixed DTMB 5512 hull with a servo-needle-type wave probe, including uncertainty analysis. Maury et al. (2003) used a circulation tunnel and resistive-type wave probe with forced harmonic motion with a Wigley and series 60 hull. Lugni et al. (2013) measured the wave pattern around a fixed DTMB5415 hull with a capacitance-type wave probe. Recently, Kim et al. (2017) measured the wetted surface elevation near a liquified-natural-gas(LNG) carrier model in waves and compared the results with numerical computation.

In the present research, the wave elevations around ship are measured for two different ships, aiming the analysis of unsteady wave elevation components, and the measured data are compared with the results of numerical computation. The ship models are very different: a ship with mathematical hull and an actual LNG ship. The existing results show the possibility of collecting reliable unsteady wave data for analysis or validation purposes. Image processing methods such as Shigeru et al. (1998) are promising for the methods mentioned above; however, light scattering, diffusion, or light source control under breaking conditions is imperfect in the current towing tank test system. Contact-type wave probes have an intrinsic possibility of unintended disturbance on unsteady waves. Meanwhile, the mean position change and motion variation in waves is an important parameter for disturbed wave elevation. To this end, unsteady wave analysis for a vertical motion-free model is performed using a non-contact measurement device. Measurement is carried out based on non-contact ultrasonic sensors with a Cartesian body-fixed coordinate system. A series of experimental analyses is performed to reveal the nonlinear characteristics and build up a rich source of database. The main topic of this study is the analysis of linear and nonlinear components of waves in harmonic head waves. In addition, the dynamic and kinematic characteristics of a rigid ship in waves and the unsteady wave components are compared. Repeatability test for unsteady wave components shows reasonable bands of the measurement. Based on the Fourier transform, the measured signals are decomposed into mean, linear, and nonlinear harmonic series. The characteristics of unsteady disturbed waves in regular head waves are examined for various wave conditions with different nonlinearity levels. During this process, some important characteristics are observed, and comparison between steady waves in deep and calm water and the time average of unsteady waves in regular waves is performed. In addition, validation examples with linear computation results using the Rankine panel method are shown.

2. Analysis method

Unsteady wave elevation can be measured during the standard towing tanks including a resistance test and self-propulsion test both with and without incident waves. Each towing-tank test method is well described in the (ITTC, 2014, 2017a; 2017b), and seakeeping tests done in the towing tank at Seoul National University are summarized in Lee et al. (2017), Park et al. (2015), and Lee et al. (2018), but the measurement of wave elevation requires additional effort from the experimental procedures for hydrodynamic forces and motion responses. In this section, only the measurement of wave elevation is explained.

Let's consider a right-hand Cartesian coordinate system as shown in Fig. 1. The variable U is the advancing speed, L is the length between perpendicular of the model, and $\zeta(x,y,t)$ is the instantaneous free surface elevation at position (x,y) and time t. The origin of the coordinate system lies on the midship of the model, center of the model, and on the undisturbed free surface. Ultrasonic sensors are placed within a range which grid covers from the bow to the stern area ($-0.7<x/L<0.7$, $0<y/L<0.28$), which includes up to 840 discrete measurement points. For one wavelength, a minimum 15 to 30 spatial grid is included. Fig. 1 shows the two grid systems: the locations of elevation sensors in the towing-tank experiment and the solution grids for numerical computation which will be described later. The measurement frequency is 40 Hz, which is sufficient to capture the considered signals.

The target variables achieved in this study and their functional relationship between target variable and related parameters are summarized in Eqs. (1)–(5). The measured free surface elevation in unsteady conditions can be broken down into mean (0-th), linear (1-st), and higher (2-nd, 3-rd, and so on) harmonic components plus residual components, as in Eq. (5). Fourier transform or Fourier series with the least squares method is used in this decomposition process.

$$\text{Heave motion RAO: } \xi_3' = \xi_3/A = f(A,U) \tag{1}$$

$$\text{Pitch motion RAO } \xi_5' = \xi_5/kA = f(A,k,U) \tag{2}$$

$$\text{Added resistance : } R_{aw} = \frac{R_W - R_{SW}}{\rho g A^2 B^2/L} = f(U, R_{SW}, R_W) \tag{3}$$

$$\text{Undisturbed wave elevation } \zeta_a(t) = \sum_{n=0}^{\infty} \zeta_{a,n} e^{in\omega_e t + \varepsilon_{a,n}} = f(x,y,t,A,\omega_e,U) \tag{4}$$

Disturbed wave elevation:

$$\zeta_A(x,y;t) = \frac{\zeta(x,y;t)}{A} = \sum_{n=0}^{\infty} \frac{\zeta_n}{A}(x,y) e^{in\omega_e t + \varepsilon_n} + \text{Res.} \cong \sum_{n=0}^{3} \frac{\zeta_n}{A}(x,y) e^{in\omega_e t + \varepsilon_n} + \text{Res.} = f(x,y,t,A,\omega_e,U) \tag{5}$$

Here, ξ_3 is the linear heave motion amplitude, ξ_5 is the linear pitch motion amplitude, B is the ship breadth, ρ is the water density in the towing tank, ω_e is the encounter frequency between the model and incident waves. Furthermore, k is the wave number, $\zeta_{a,n}$ is the n-th order harmonic amplitude of an undisturbed wave, A is the 1st order (linear) wave amplitude, i.e. $A \equiv \zeta_{a,1}$, ζ is the total disturbed wave, ζ_n is the elevation of n-order wave component, R_W is the time-average value of resistance in a wave, R_{SW} is the calm water resistance, and R_{aw} is the non-dimensional wave resistance, respectively.

In the present study, the towing tank experiment has been carried out at the towing tank of Seoul National University, which is 110-m long, 8-m wide, and 3.5m deep and has a wave maker with 8 flaps. Fig. 2 shows the experimental scheme and wave measurement system used in this study, and the measurement parameters of devices are listed in Table 1. Although motion responses and added resistance in waves are measured simultaneously, this paper focused on the observation of unsteady wave components, and a more thorough investigation related to motion response, added resistance, mean position, and other wave elevation components near the hull can be delivered through another paper.

Wave elevations around the ship hull have been measured by using an array of 4 × 2 ultrasonic sensors. Due to the limited number of

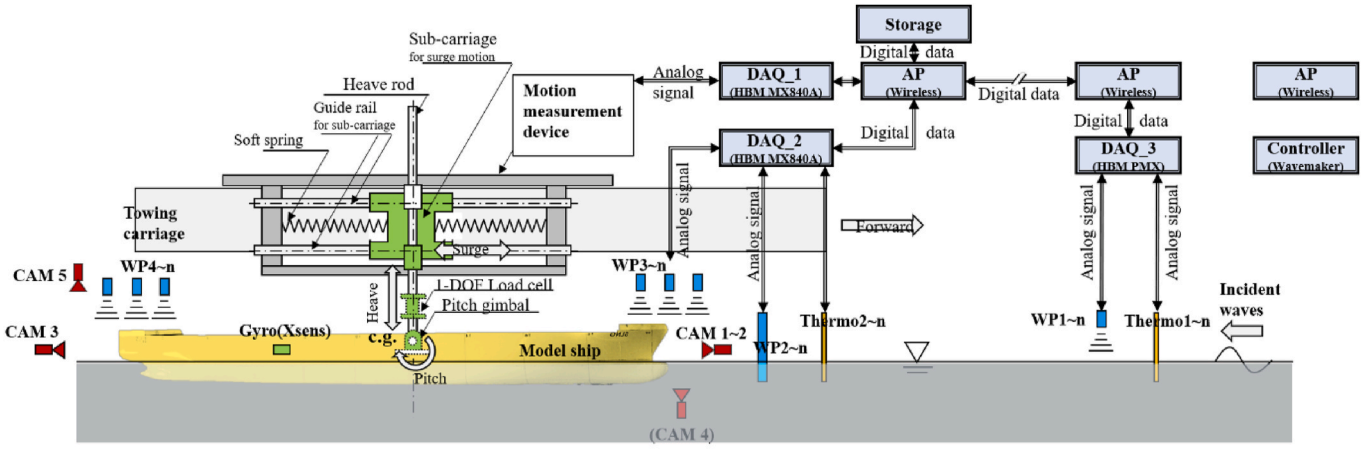

(a) Measurement system for towing test

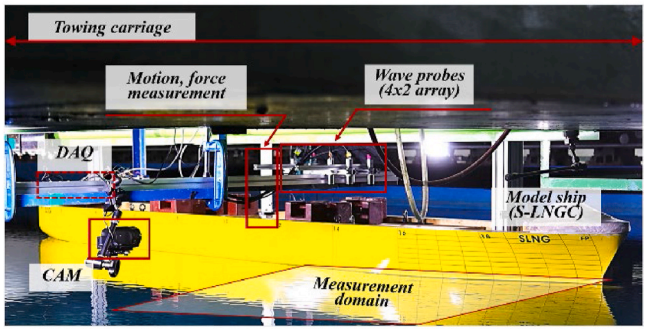

(b) Side view

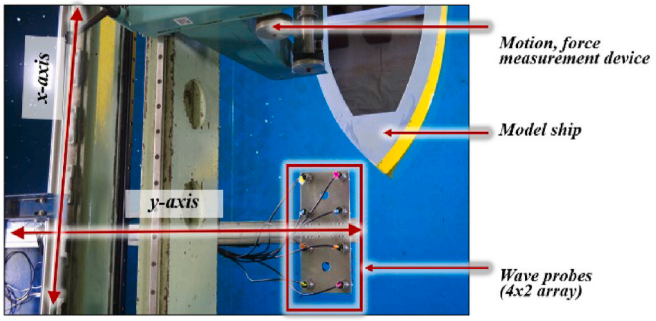

(c) Upper view

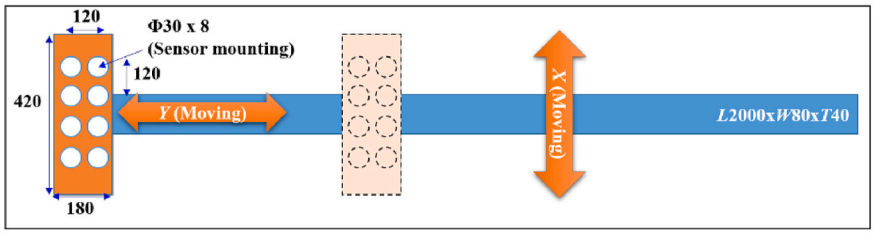

(d) Guidance system for wave probe arrays

Fig. 2. Experimental scheme and wave probe array in captive model system.
(a) Measurement system for towing test
(b) Side view (c) Upper view
(d) Guidance system for wave probe arrays.

Table 1
Measured parameters and devices properties.

Item	Device type (Model name)	Resolution Accuracy (% of full scale)
Undisturbed wave elevation (fixed near wave maker)	Ultrasonic (Senix TS-30S1)	0.12 mm 0.50 mm (0.1%)
Undisturbed wave elevation (moving with the towing carriage)	Ultrasonic (Senix TS-30S1)	0.12 mm 0.50 mm (0.1%)
Disturbed wave elevation near the model (8 points)	Ultrasonic (Senix TS-30S1)	0.12 mm 0.50 mm (0.1%)
Longitudinal dynamic force on model	Strain-gauge type load cell (Wonbang MCL-1A03-50)	0.025 *N* (0.05%)
Kinematic displacement of the model	Potentiometer (CPP-45)	0.35 *deg.* (0.1%)
Water temperature	Thermocouple (IRtek IR50i)	0.1 °*C* 1.0 °*C*
Digital data acquisition from analog sensors (DAQ)	Data acquisition system (HBM MX840A)	**24 bits resolution for analog to digital conversion*

sensors, many repeat runs should be performed to characterize the full wave pattern. More importantly, there is interaction between the sensors when they are too close. This is a limitation factor in the arrangement of the sensors. During these repeat tests, up to three different position sets were achieved in single run. Considering the incident wave characteristics and towing tank dimension, Benjamin-Fier instability (Benjamin and Feir, 1967) should be considered in this type of the test. In other words, the wave amplitude and phase modulation should be considered in a long towing tank. Normalization with a measured incident wave tracking the model can solve this problem; this normalization issue will be discussed in the following section. The position of the fixed wave probe near the wave maker was set at 11 *m* from wave maker, considering the wavelength of local evanescent mode. The blockage effect was determined based on ITTC 2017 (ITTC, 2017b), and the experimental conditions were considered to minimize the blockage effects in seakeeping test. The waiting time was set to be regular for the same wave conditions, between 15 and 20 min, according to wave height. The water temperature was 24.4 °*C*, and the temperature variation was less than 1.0 °*C* throughout the entire measurement. Analysis of the experimental data was based on ITTC (2014; 2017a), and more details are summarized in Lee et al. (2018).

Uncertainty must be mentioned in towing tank experiment. As well known, the uncertainty analysis of seakeeping experiment is not simple, since the uncertainty level is a function of multiple parameters, e.g. wave amplitude and frequencies, ship speed, and load conditions. Many repeated tests are essential for each wave condition, but it is very hard to carry out numerous tests in practical point of view. This experiment is a follow-up experiment of Park et al. (2015) which adopts the procedure of ITTC (ITTC, 2017b), therefore their uncertainty analysis is valid for this seakeeping experiment.

It should be mentioned that the wave pattern radiating from a ship is dependent on the Brard number, s.t. $\tau = U\omega_e/g$ where ω_e indicates the encounter wave frequency. As well known, the wave patterns are different when τ is greater than 0.25 or smaller than 0.25, and the difference of such cases due to the propagation speed of the group velocity of the waves generated by the ship motion, and details can be found in

Table 2
Principal dimensions of test models.

	Unit	modified Wigley	S-LNGC
Length between perpendiculars (*L*)	*m*	3.000	4.000
Breadth (*B*)	*m*	0.600	0.621
Draft (*d*)	*m*	0.210	0.159
Displacement Volume (∇)	m^3	0.2407	0.3033
Radius of gyration (k_{yy}/L, k_{zz}/L)	–	0.236	0.233
Block coefficient (C_B)	–	0.634	0.770
Vertical center of gravity (*KG*)	*m*	0.173	0.234
Longitudinal center of gravity (*LCG*) (from midship to forward+)	*m*	0.000	−0.037
Vertical center of buoyancy (*KB*)	*m*	0.121	0.083
Longitudinal center of buoyancy (*LCB*) (from midship to forward+)	*m*	0.000	−0.034
Radius of gyration (k_{yy}/L)	*m*	0.236	0.233
Sinkage	*m*	0.000	−0.0048
Trim (fore/aft, +: bow goes down)	*m*	0.000	−0.0606

Table 3
Test conditions for modified Wigley model.

(a) Calm water test

Item	Magnitude
Fn	0.15/0.20
Motion allowed	Vertical free (heave, pitch, surge)

(b) Regular head sea conditions with motion (λ: wavelength, *H*: wave height)

Item		Magnitude			
Fn	0.15	0.20			
λ/L	0.4	0.3	0.4	0.5	0.6
H/λ	0.025	0.025	0.013, 0.025(*1) 0.038	0.025	0.025
kA	0.079	0.079	0.039 0.079 0.118	0.079	0.079
H/L	0.010	0.008	0.005 0.010 0.015	0.013	0.015

(*1. Underline condition means that the measurement coverage includes full bow and stern part; otherwise, measurement covers bow part.).

Fig. 3. Test models: blunt modified Wigley(upper), S-LNGC(lower).

Table 4
Test conditions for S-LNGC model.

(a) Calm water test			
Item			Magnitude
Fn			0.188
Motion freedom			Vertical free (heave, pitch, surge)
b) Regular head sea conditions with motion (λ: wavelength, H: wave height)			
Item	Magnitude		
Fn	0.188		
λ/L	0.3	0.4	0.5
H/λ	0.025	0.013	0.025
		0.025	
		0.038	
kA	0.079	0.039	0.079
		0.079	
		0.118	
H/L	0.008	0.005	0.013
		0.010	
		0.015	

many existing references (e.g. Faltinsen, 1990).

In this study, all the wave conditions are greater than 0.25. However, the present measurement is done in local area around ships, and the decomposition of wave direction and pattern is beyond of this research. That is, the analysis is carried out focusing on for steady, mean, and *n*-th order harmonic components.

3. Ship model and test conditions

Two ship models are considered in this study: a real ship hull and a mathematical hull. The former is the S-LNGC (Kim et al., 2017; Kim et al., 2019) provided by Samsung Heavy Industry, and the other is a blunt modified Wigley hull which is defined as Eq. (6) (Kashiwagi 2013; Yang et al., 2020).

$$\overline{y}=(1-\overline{z}^2)(1-\overline{x}^2)(1+0.6\overline{x}^2+\overline{x}^4)+\overline{z}^2(1-\overline{z}^8)(1-\overline{x}^2)^4, \overline{x}=x\frac{2}{L}, \overline{y}=y\frac{2}{B}, \overline{z}=\frac{z}{d} \quad (6)$$

Here, d is the ship draft. For the modified Wigley hull form, the vertical wall side is set above the mean water level, while the S-LNGC model has a practical hull shape including a bow flare, bulbous bow, and transom stern(see Fig. 3). The main dimensions are listed in Table 2, and each model is set to satisfy the original target parameter within the 3% error.

Test conditions for the modified Wigley in calm water and in waves are listed in Table 3. For representative cases, which are emphasized in Table 3 (**1*), measurements were performed over the entire range (*-0.7 < x/L < 0.7*); otherwise, measurements were focused on the bow range (*0.1 < x/L < 0.7*). Test conditions for the S-LNGC in calm water and in waves are listed in Table 4. Measurements were conducted for the bow range (*0.1 < x/L < 0.7*), and non-dimensional wave conditions were set to be similar to those used for the modified Wigley model. Towing speed was constant at the designed speed. The surge, heave, and pitch motions were set to be free, and a soft spring system of 380 N/m was adopted for the surge motion of the ships. The details about the soft spring can be found in the paper of (Lee et al., 2017).

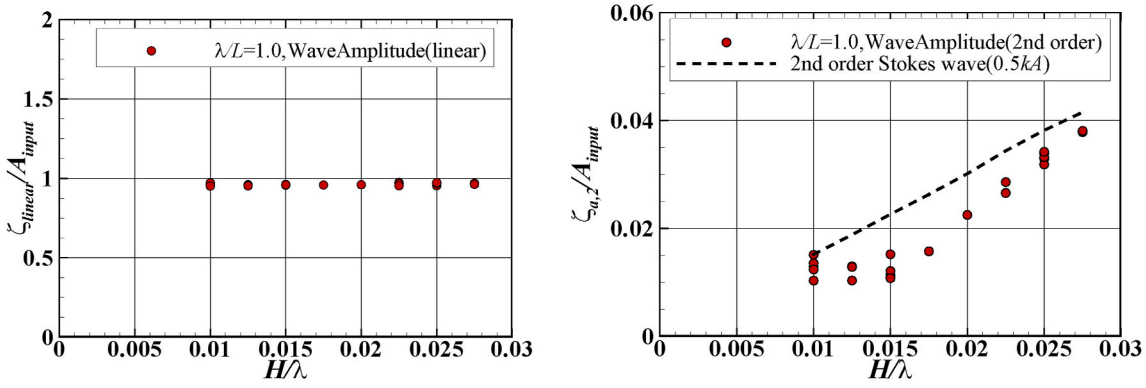

(a) First harmonic amplitude (b) Second harmonic amplitude

Fig. 4. Amplitudes of incident waves for various wave slopes: H/λ = 1/100–1/36. (a) First harmonic amplitude (b) Second harmonic amplitude.

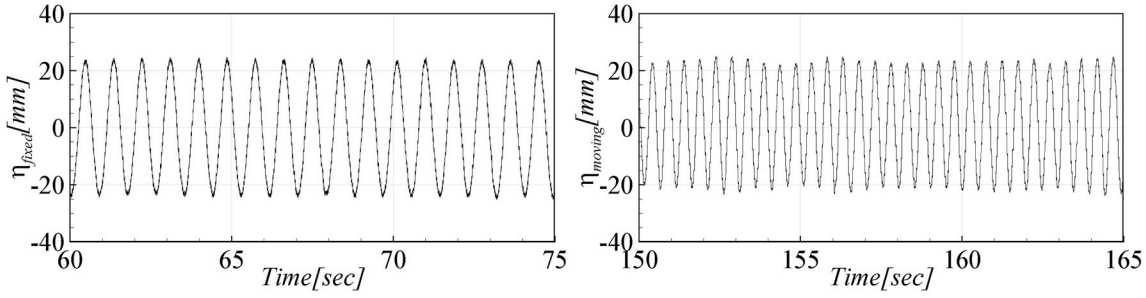

(a) From wave probe near wave maker (b) From wave probe moving with towing carriage

Fig. 5. Incident wave signals measured at two locations (η_{fixed} vs. η_{moving}) (a) From wave probe near wave maker (b) From wave probe moving with towing carriage.

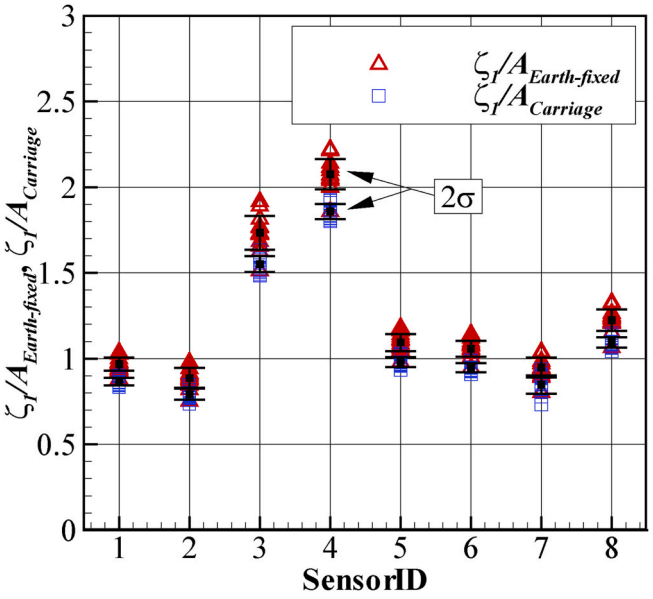

Fig. 6. Comparison of normalized wave amplitudes and standard deviation (2σ) for the 1-st harmonic component based on 14 repeated tests: Blunt Wigley hull, $Fn = 0.2$, $H/\lambda = 1/40$, $\lambda/L = 0.4$, disturbed wave elevation.

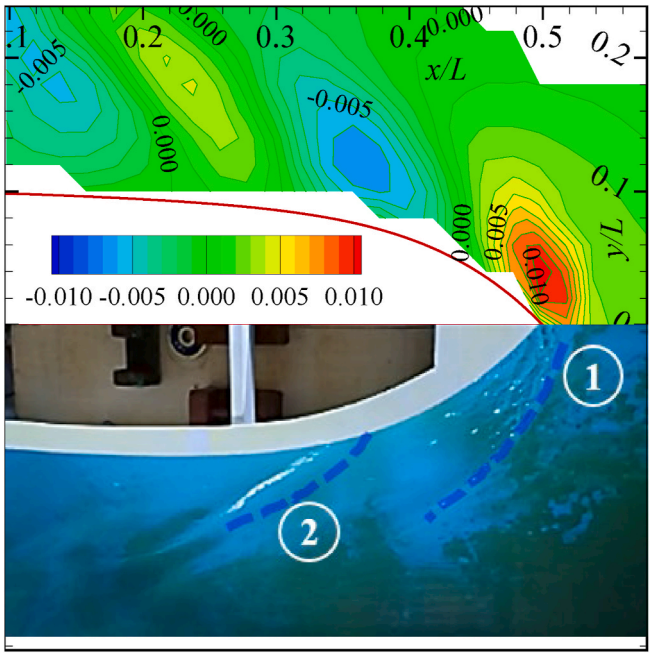

Fig. 7. Steady wave elevation near bow at $Fn = 0.2$ (upper: measured (ζ_0/L), lower: photogrammetry).

4. Sensitivity study for wave elevation measurement

Confirming the uniformity of the undisturbed incident wave is important. To this end, several parameters can be checked: the frequency of the incident wave ω, the first and second harmonic amplitudes $\zeta_{a,1}$ and $\zeta_{a,2}$, and spatial modulation along the advancing direction. As

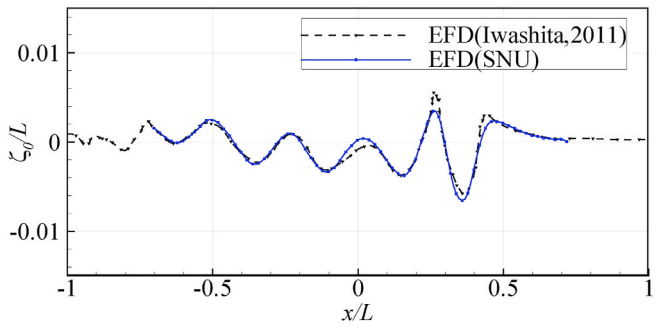

Fig. 8. Comparison of the zero-th order wave elevation with an existing data: wave cut on $y/(B/2) = 1.4$, blunt Wigley hull, $Fn = 0.2$.

the amplitude of generated wave increases, a careful check is required particularly for higher-order components since their magnitude becomes larger.

Fig. 4 shows the repeatability of the first and second harmonic amplitudes of incident waves. Here, the results are normalized based on the 'input' wave amplitude. The normalized wave amplitudes are approximately 0.97, which means that the linear amplitudes of generated waves are about 3% lower than the input value (see Fig. 4 (a)), and this repeatability of the wave generation seems acceptable for the present analysis. The magnitude of the second harmonic follows the 2nd-order Stokes wave theory, but the standard deviation of the second harmonic component is higher than that of the first harmonic component. Therefore, careful treatment is needed for analyzing the non-linear parts in the small-scale model test. Based on the present observation, the overall repeatability of incident waves is in a reasonable range.

Spatial modulation of the waves also should be considered during the towing tank test. As described by Lake et al. (1977), modulation of the wave propagation along the longitudinal towing tank can be observed because of side wall friction and the instability of the nonlinear wave structure. Fig. 5 shows a comparison of the measured wave signals at a fixed point near the wave maker and at the front position of the moving towing carriage. The wave signal near the wave maker shows better uniformity then the signal measured at moving carriage. This difference must be considered in the analysis of experimental data.

Fig. 6 shows an example of the normalized first-harmonic wave amplitudes which were measured at eight sensors and 14 repeated tests for the blunt Wigley hull. Each symbol represents the normalized linear amplitude of each repeated run, and the normalization was done based on the both input wave amplitude and measured wave amplitude. In this figure, $A_{Earth\text{-}fixed}$ means the wave amplitude measured at a fixed point near the wave maker and $A_{Carriage}$ is the wave amplitude measured in front of the moving carriage. This figure shows also the standard deviations of 14 values for each condition. This example shows that the suitable reliability can be achieved in the present experiment. In this study, it is hard to suggest any procedure which is more appropriate in the choice of reference wave elevation for normalization. Therefore, this issue must be studied in a more systematic manner.

5. Results and discussions

5.1. Steady wave and mean wave components

The results of this study are displayed in several different manners, including instant wave contours and amplitude contours. Fig. 7 shows the elevation contour normalized by the ship length, ζ/L, near the bow

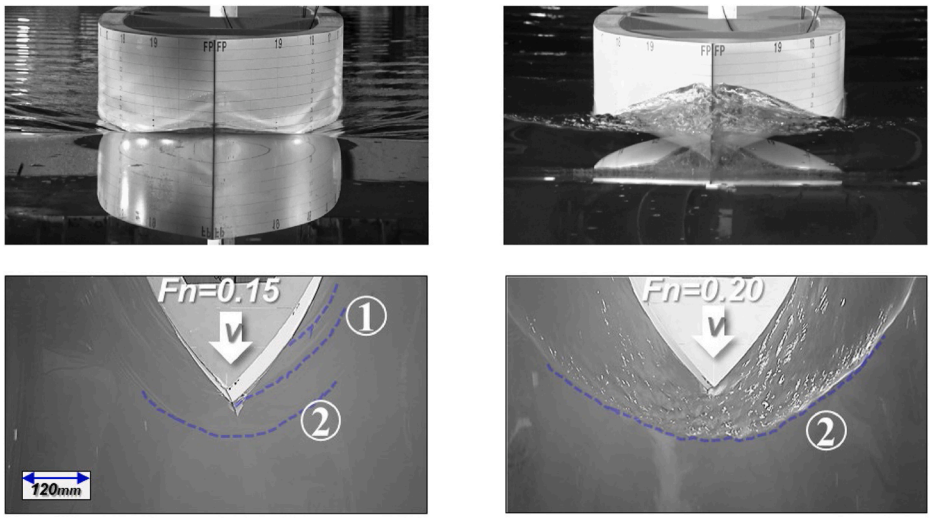

(a) *Fn*=0.15 (b) *Fn*=0.20

Fig. 9. Photometry for bow waves under calm water conditions: blunt Wigley hull.
(a) *Fn*=0.15 (b) *Fn*=0.20.

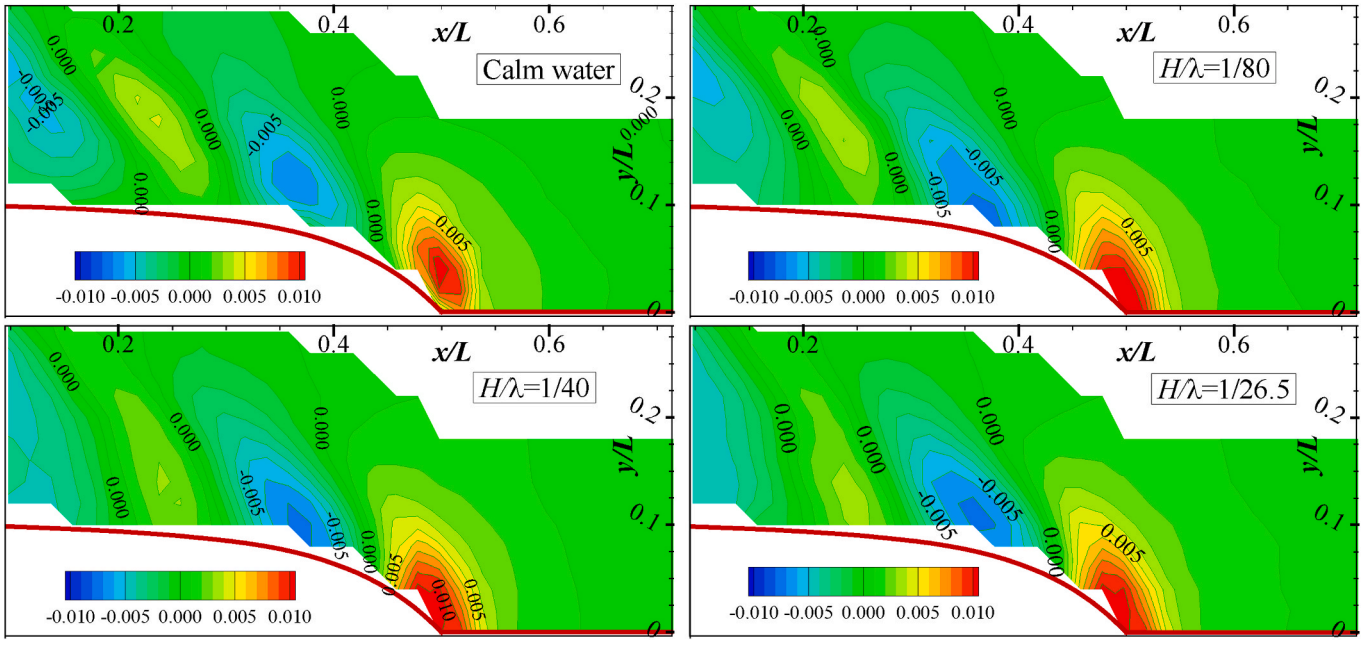

Fig. 10. Steady wave component vs. mean components of unsteady wave amplitude for different incident wave slopes (H/λ): blunt Wigley hull, Fn = 0.20, λ/L = 0.4.

($0.1<x/L<0.7$) of the blunt Wigley hull in calm water condition. This modified Wigley hull is not optimized for hydrodynamic performance, and significant wave breaking and wake are observed(see ① in Fig. 7). The measured wave pattern captures well the largest peak near the bow front (see Fig. 7, upper). Around the ship shoulder, a wave trough line is shown in the photo(see ② in Fig. 7). Overall, the measured wave amplitude describes well the characteristics of bow waves under steady conditions. In addition, the wave cut at $y/B = 0.7$ for the steady wave is compared with published wave cut analysis data (Iwashita et al., 2011; see Fig. 8) which used a 2.5-m ship model. The wave length and bow and stern peak amplitudes are very similar despite some difference in crest and trough. Differences between the published paper and this study may come mostly from the difference of measurement scheme and resolution of elevation measurement.

Breaking waves are clearly visible for $Fn = 0.20$, while not much breaking occurs for $Fn = 0.15$ (see Fig. 9). For $Fn = 0.2$, breaking is so

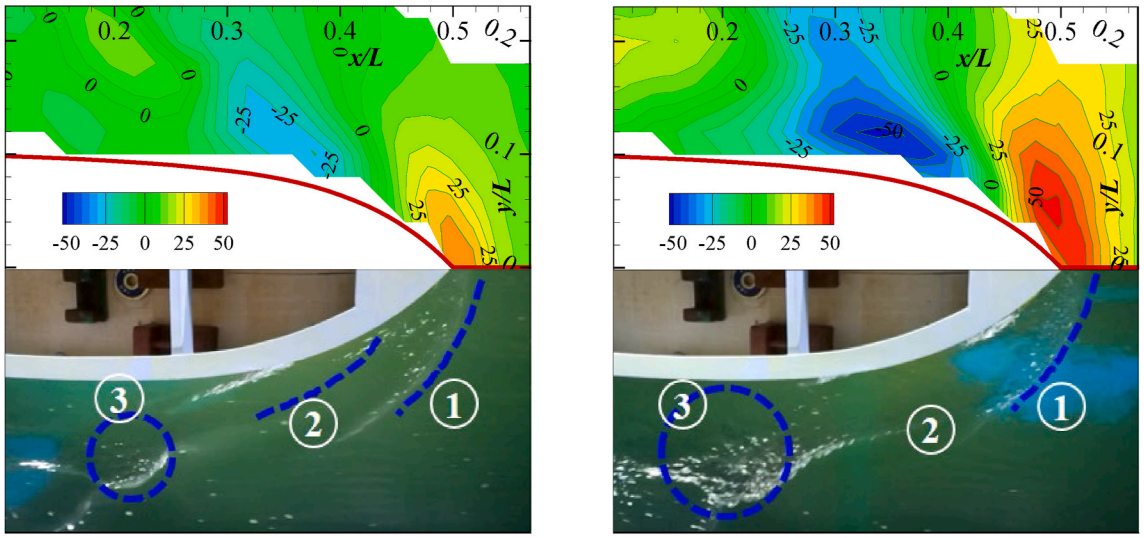

(a) H/λ=1/80 (b) H/λ=1/26.5

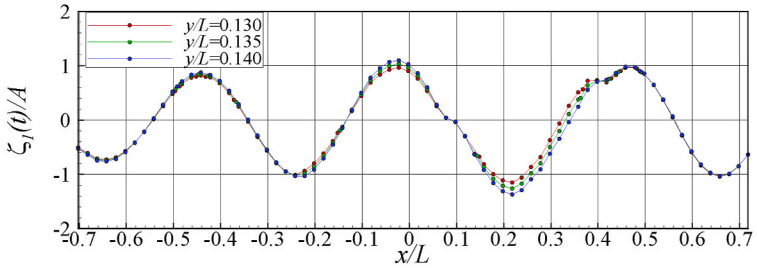

(c) First harmonic instantaneous wave cut comparison for y/L=0.13, 0.135, 0.14 (H/λ=1/26.5)

Fig. 11. Instantaneous wave elevation when wave crest is at fore-peak(FP): blunt Wigley hull, $Fn = 0.2$, $\lambda/L = 0.4$, $(\zeta_0+\zeta_1+\zeta_2+\zeta_3)$ (t_1) [mm].
(a) H/λ=1/80 (b) H/λ=1/26.5
(c) First harmonic instantaneous wave cut comparison for $y/L = 0.13, 0.135, 0.14$ ($H/\lambda = 1/26.5$).

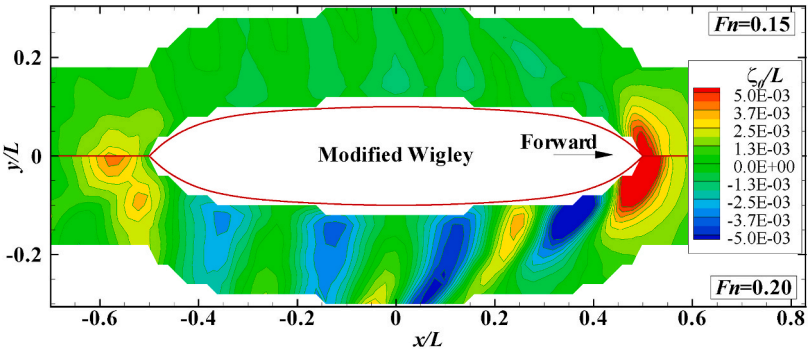

(a) Mean wave elevation component (ζ_0/L)

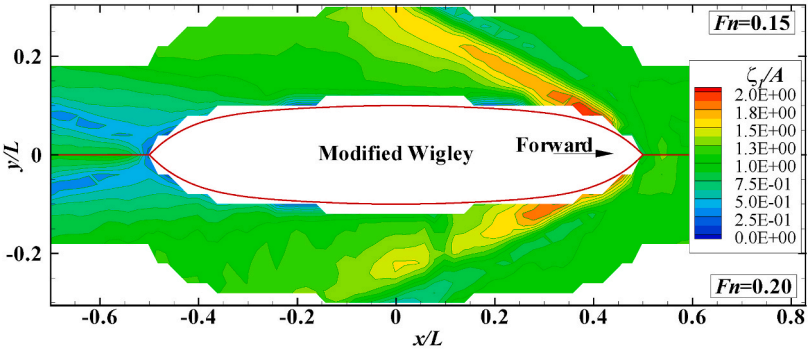

(b) First harmonic wave amplitude component (ζ_1/A)

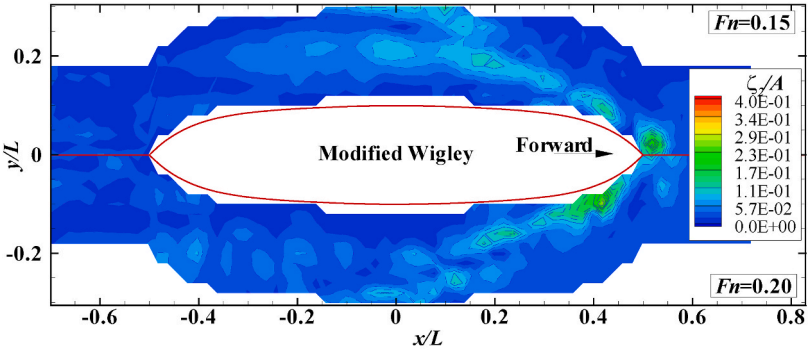

(c) Second harmonic wave amplitude component (ζ_2/A)

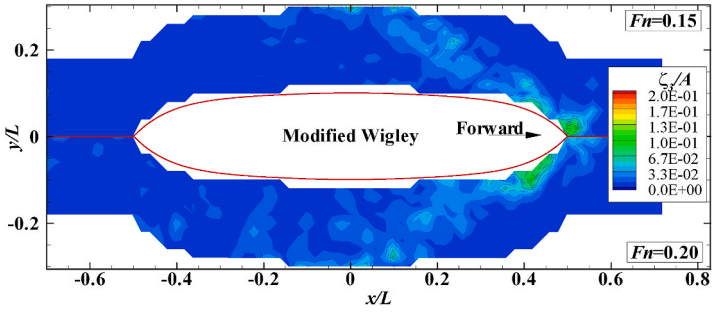

(d) Third harmonic wave amplitude component (ζ_3/A)

Fig. 12. Wave amplitude plot for various advancing speeds ($Fn = 0.15, 0.2$, $\beta = 180$ deg, $H/\lambda = 1/40$, $\lambda/L = 0.4$) (a) Mean wave elevation component (ζ_0/L) (b) First harmonic wave amplitude component (ζ_1/A) (c) Second harmonic wave amplitude component (ζ_2/A) (d) Third harmonic wave amplitude component (ζ_3/A).

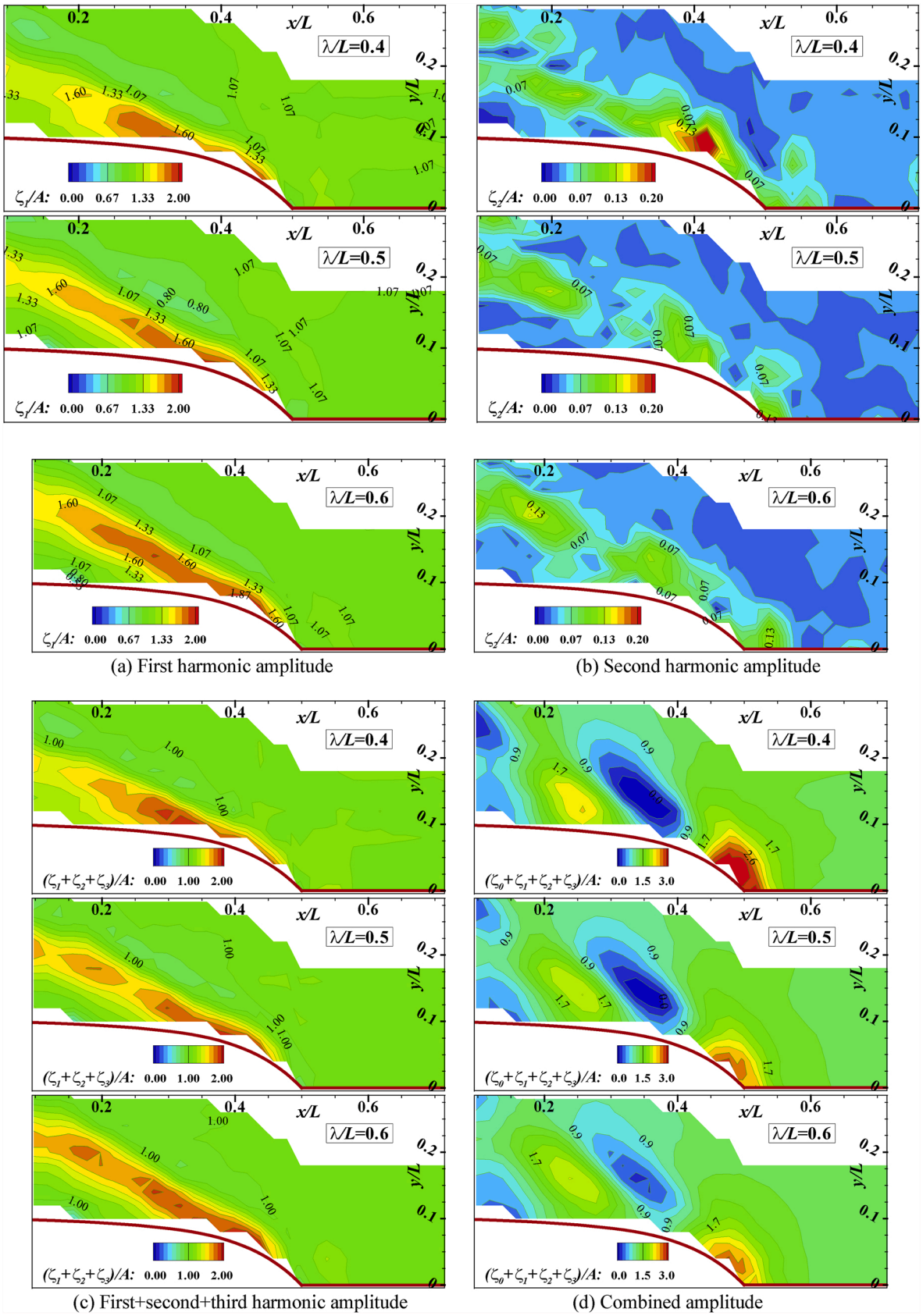

Fig. 13. Amplitudes of wave component: blunt Modified Wigley, $Fn = 0.2$, $H/\lambda = 1/40$, $\lambda/L = 0.4$–0.6.
(a) First harmonic amplitude (b) Second harmonic amplitude
(c) First+second+third harmonic amplitude (d) Combined amplitude.

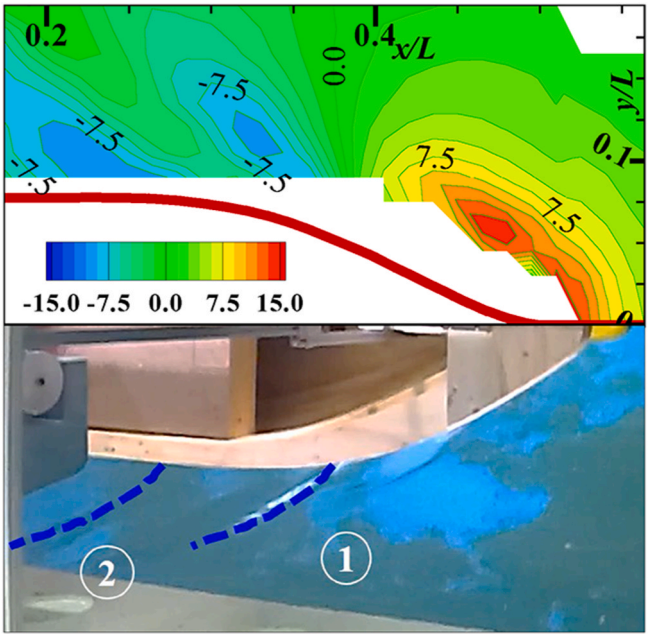

Fig. 14. Steady wave elevation(ζ_0 *[mm]*): S-LNGC, $Fn = 0.188$.

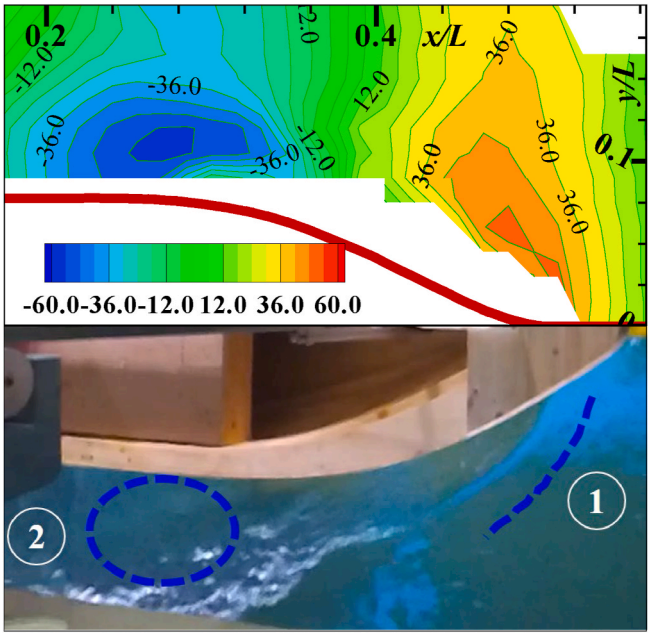

Fig. 15. Instantaneous wave elevation ($(\zeta_0+\zeta_1+\zeta_2+\zeta_3)$ (t_1)*[mm]* when wave crest located at FP: S-LNGC, $Fn = 0.188$, $\lambda/L = 0.4$, $H/\lambda = 1/26.5$.

clear that the bow and shoulder separation wave is not clearly visible, as can be seen in ① of Fig. 9. This difference affects the mean wave pattern. In this study, measurements were focused on $Fn = 0.2$, where clear nonlinear phenomena can be captured.

One interesting aspect of these results is the change in the mean wave or Kevin wake characteristics in calm water and in regular waves. The Wigley model has a vertical wall above the wetted surface; therefore, the nonlinear hull form effect on the mean wave component is expected to be lower than that of the S-LNGC. In Fig. 10, steady and mean wave contours near the bow and shoulder are divided by the ship length, *L*. The first row shows the time-averaged steady wave component in calm water, and the others show the mean wave component (zero-th order wave) analyzed from the unsteady wave component with different incident waves. In this case, slight differences can be found in the detailed comparison, but overall trends are very similar. In detail, the peaks and troughs in the presence of incident waves are smaller with respect to both range and amplitude. In short wave conditions, neither the motion nor the dynamic sinkage and trim meaningfully vary according to incident wave non-linearity. In other words, with high-frequency waves, both the ship motion and change in static position are relatively small, according to the wave amplitude variation. In addition, for the blunt modified Wigley, the bow wave is already high enough in the calm water case (see Figs. 9 and 10). Based on the above observation, it is concluded that, if there is no significant change in the position of the hull in either static or dynamic situations, the mean value of the disturbed wave near the bow does not significantly differ in waves.

5.2. Unsteady wave component

Fig. 11 (a) and (b) show the snapshots of the wave component for unsteady conditions in the physical scale. The upper figure illustrates the experimentally measured results, and the lower one presents the photometry captured during the experiment. When the incident wave crest coincides with the ship front, large pressure variation occurs and the peak amplitude can be observed. For steeper waves, as the diffracted waves go higher, more resultant breaking waves are observed(Fig. 11 (b)). Observing the wave cut near the ship hull (Fig. 11(c)), nonlinearity is strong near the bow front and shoulder parts, where disturbances are largest.

In Fig. 12, the wave amplitude contour of the entire domain ($-0.7<x/L<0.7$) is represented from the time-averaged mean value to the 3rd order harmonic. The wave amplitude plots show that the wave component is dominant around the ship bow for all components, and the stern is also important for mean wave and linear wave components. Nonlinear components are mostly important in the bow and negligible in the stern. Furthermore, speed effects are dominant for the mean wave component, and less effective for the first and harmonic waves.

For the parametric study, the wave components near the bow are compared for different wave lengths in Fig. 13. According to this result, it seems that the first harmonic wave amplitude (ζ_1/A) is a little affected by the wave length. As the wavelength increases, the wave intensity and propagation angle become stronger and wider. The diverging angle for the 2nd-order component also changes, although the magnitude is not high. The combined elevation in Fig. 13(d) shows the relative importance of the mean and first harmonic wave components for different wave conditions. Particularly, it shows that the wave elevation non-dimensionalized by incident wave amplitude becomes weaker as the length is shorter.

5.3. Comparison of different hull forms

In the case of experiment for the S-LNGC hull, the incident wave conditions and measurement domain are similar to those for the modified Wigley model, but the elevation sensors could not be installed close

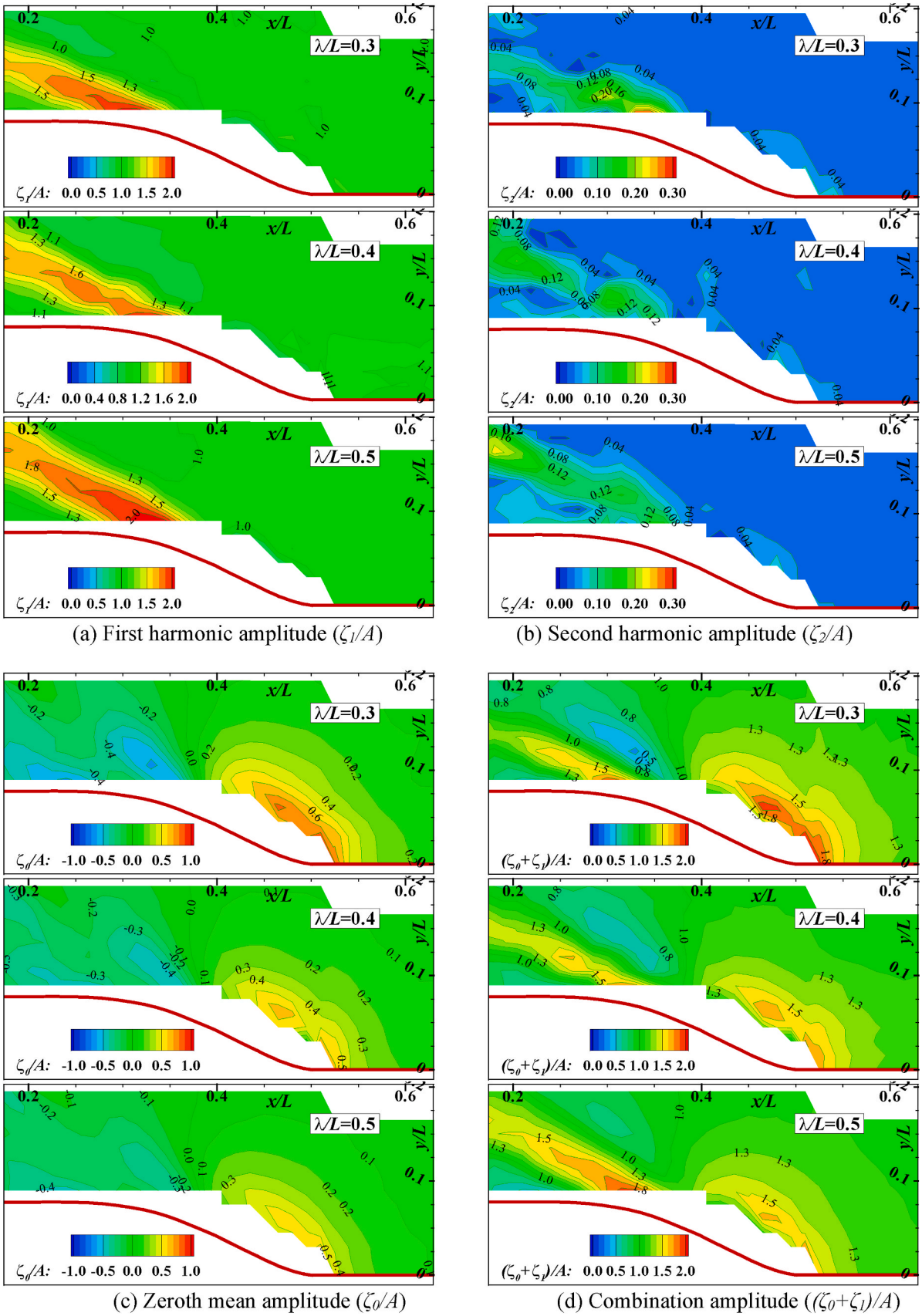

(a) First harmonic amplitude (ζ_1/A) (b) Second harmonic amplitude (ζ_2/A)

(c) Zeroth mean amplitude (ζ_0/A) (d) Combination amplitude ($(\zeta_0+\zeta_1)/A$)

Fig. 16. Wave amplitude plots for different incident wave length: S-LNGC, $Fn = 0.188$, $H/\lambda = 1/40$, $\lambda/L = 0.3$–0.5(a) First harmonic amplitude (ζ_1/A) (b) Second harmonic amplitude (ζ_2/A) (c) Zeroth mean amplitude (ζ_0/A) (d) Combination amplitude ($(\zeta_0+\zeta_1)/A$).

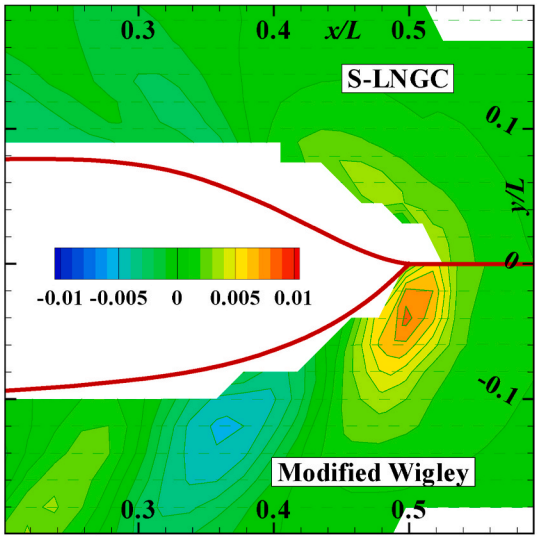

(a) Steady wave elevation (ζ_0/L)

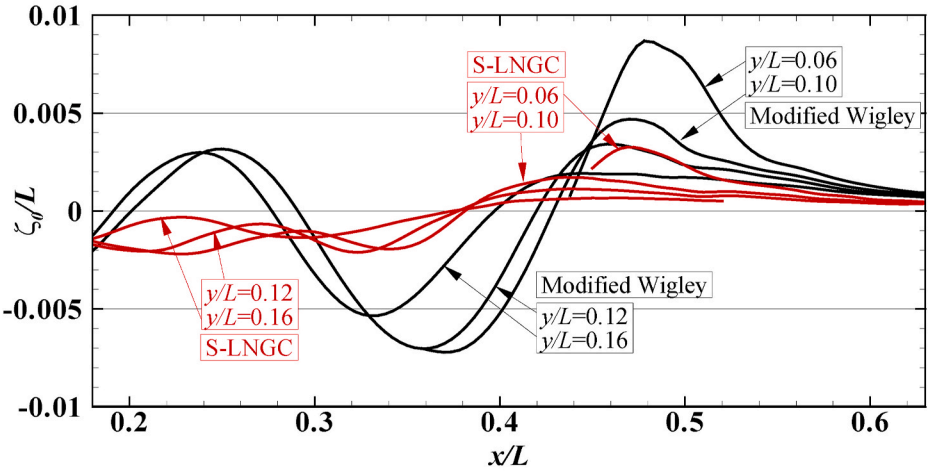

(b) Longitudinal steady wave cut

Fig. 17. Comparison of wave contour and wave cut in calm water condition: $Fn = 0.188$ for S-LNGC, $Fn = 0.2$ for blunt Wigley hull.(a) Steady wave elevation (ζ_0/L) (b) Longitudinal steady wave cut.

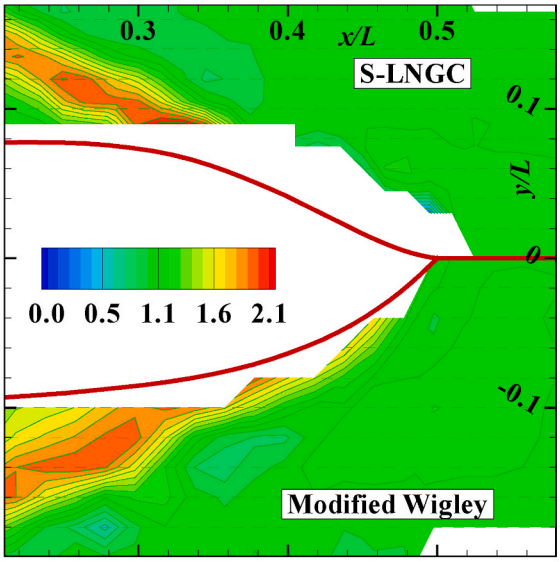

(a) First harmonic wave amplitude (ζ_1/A)

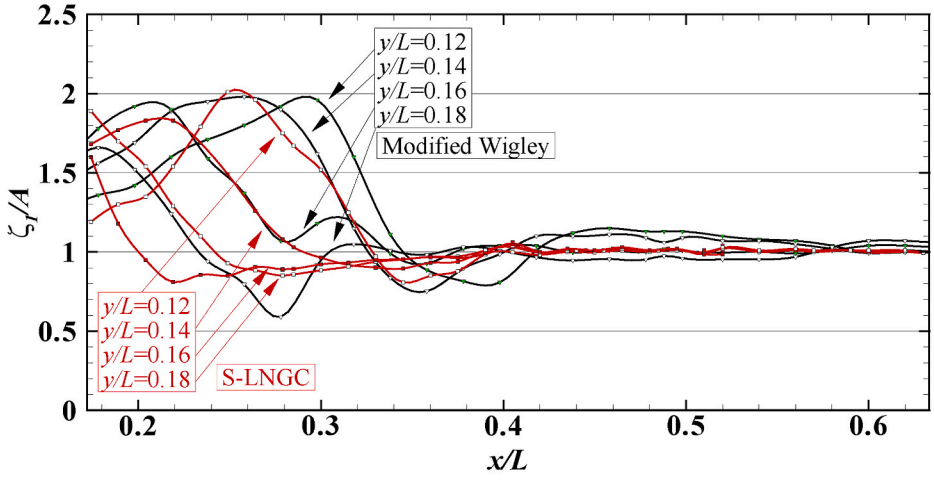

(b) Longitudinal cut of first harmonic wave amplitude

Fig. 18. Comparison of wave contour and wave cut of first harmonic component: $Fn = 0.188$ for S-LNGC, $Fn = 0.2$ for blunt Wigley hull, $\lambda/L = 0.4$, $H/\lambda = 1/80$.(a) First harmonic wave amplitude (ζ_1/A) (b) Longitudinal cut of first harmonic wave amplitude.

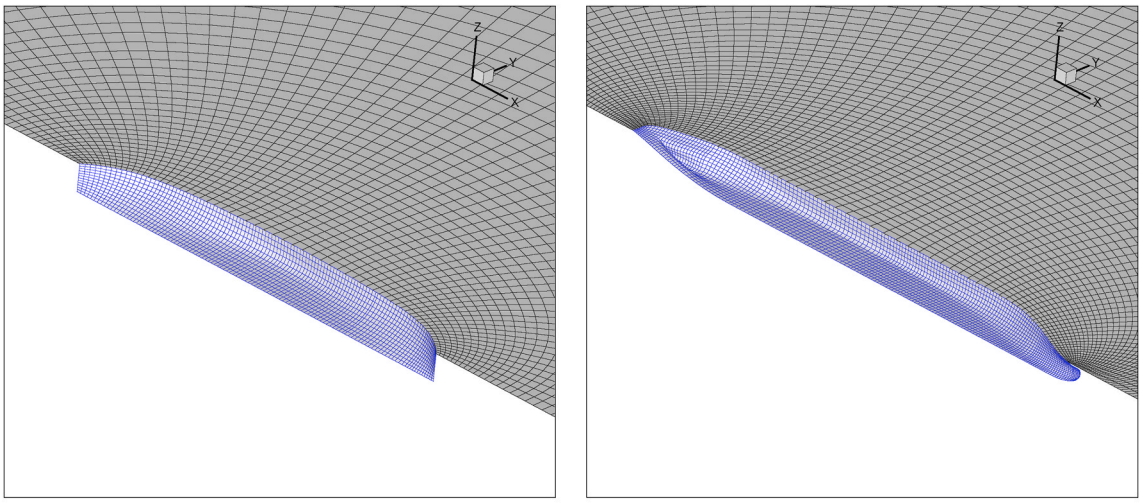

Fig. 19. Solution panel for the numerical computation (blue: hull mesh, black: free surface mesh) (
a) blunt Wigley (b) S-LNGC. (For interpretation of the references to colour in this figure legend, the reader is referred to the Web version of this article.)

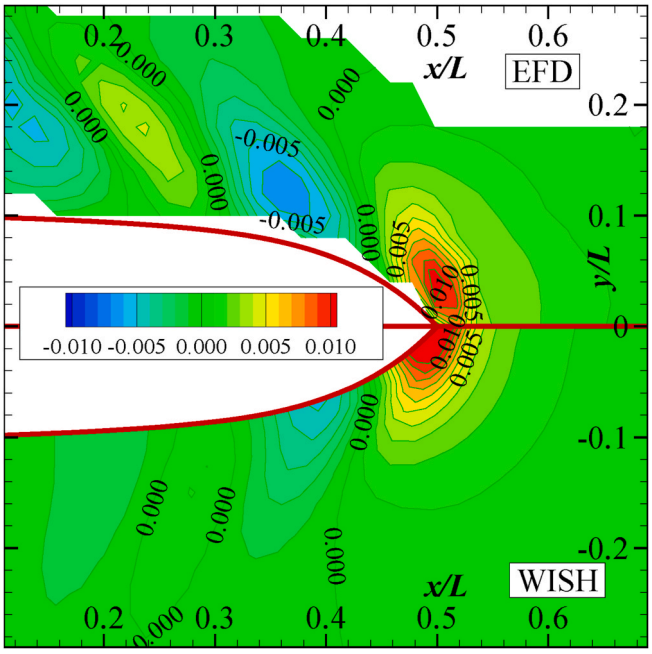

Fig. 20. Comparison of steady wave elevation (ζ_0/L): experiment (upper) vs. linear computation (lower), blunt Wigley hull, $Fn = 0.2$, calm water.

to the hull surface as much as the blunt Wigley hull due to the flare above the still water level. Fig. 14 shows that the steady wave elevation around the S-LNGC hull for $Fn = 0.188$. Here, the red line shows the waterline in calm water, and the photo shows an upper deck flare. Fig. 15 shows instantaneous wave elevation combination of the harmonic components up to the 3-rd order. As expected, the reconstructed elevation shows good consistency with snapshots. Fig. 16 represents the harmonic amplitude plot for various wave periods, and the overall trend is similar to that of the blunt Wigley hull. However, there must be small difference due to different waterline profile and sectional profiles between the two ships. Unfortunately, the wave elevation close to the ship bow is unavailable, therefore the detailed difference near bow cannot be clearly observed.

From the observation on the results for the S-LNGC and blunt modified Wigley hull forms, several clear differences can be found. The modified Wigley model has a vertical side wall above the mean waterline, and the S-LNGC has bow flare and transom stern parts. In addition, the modified Wigley has no bulb, and significant wave breaking occurs. In steady wave conditions, the modified Wigley caused a far larger wave to form around the bow hull form (see Fig. 17 (a)). In Fig. 17 (b), the wave cuts for various positions (y/L) are compared for each hull form, and the dotted line in Fig. 17 (a) depicts locations. The first peak value is

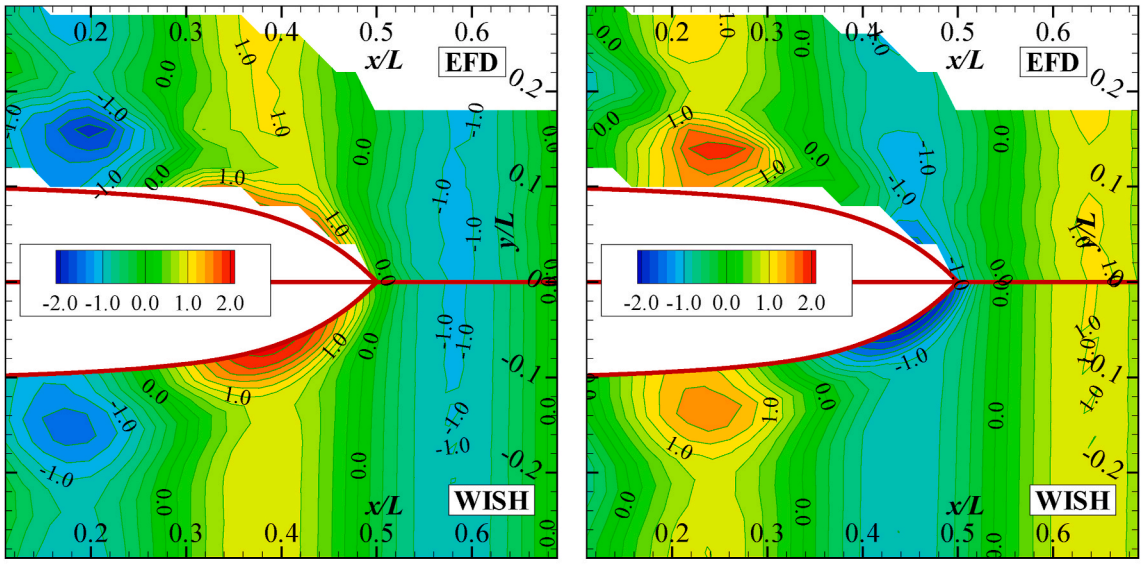

Fig. 21. Comparison of the first harmonic component of instantaneous wave elevation ($\zeta_1(t)/A$): experiment vs. linear computation, blunt Wigley hull, $Fn = 0.2$, $\lambda/L = 0.4$, $H/\lambda = 1/80$ in experiment, T_e: encounter wave period.
(a) $t = t_1+T_e/4$ (b) $t = t_1+T_e/2$.

nearly three times larger, even for the side position ($y/L = 0.06$, see Fig. 17 (b)), and the following trough and second peak are also several times larger for the modified Wigley. These differences are obviously partly due to the difference of ship speed, and also partly due to the bulb effect of the S-LNGC and the concave shape of the bow. Furthermore, the wave length for the blunt Wigley appears to be shorter than that of the S-LNGC in Fig. 17 (a). For the first harmonic wave amplitude, the reflection angle is similar for the two hull forms, and the peak amplitude is similar under the same wave conditions. In these conditions, the ship motions in the vertical plane are small; therefore, the diffraction component is dominant for unsteady waves. The detailed disturbance range and intensity of the 1-st harmonic amplitude for the S-LNGC are smaller (see Fig. 18), which may be due to the efficient hull shape of the S-LNGC. However, the direct comparison of the two ships must be cautious since the Froude numbers are slightly different.

6. Comparison with computational solutions

Computational results are compared with the measured wave components. The numerical wave component is obtained by solving the linear potential problem based on the Rankine panel method. Particularly, the WISH program developed at Seoul National University (Kim and Kim, 2009, 2011, 2011; Lee et al., 2017) has been applied. The WISH program is a well-known program for seakeeping analysis, which adopts the B-spline scheme for velocity potential and wave elevation. This program solves the linear, weakly nonlinear and weak-scatterer problems for the motion responses and wave loads on ships and structures. Since many papers about the application of the WISH program were already published, the details are not included in this paper. An example of solution panels is shown in Figs. 1 and 19, and other conditions are set to be same as those used in the experiments. Three comparison sets include the steady wave component in calm water, instantaneous wave contour at different time instants, and linear wave amplitude contours.

In Figs. 20–23, comparison results for the blunt Wigley are shown. According to Fig. 20, the measured steady wave component is slightly larger, and the wavelengths in downstream from the ship shoulder are a little different. As described above, the waves around this ship have significant nonlinearities such as wave breaking, therefore some discrepancy with the computational results based on linear boundary value problem is inevitable. However, the agreement of overall wave pattern is obvious. Fig. 21 shows two instantaneous elevation contours in regular wave conditions. Like the steady wave case, the agreement of overall wave pattern between experiment and computation is very clear.

Figs. 22 and 23 represent the amplitude contours of unsteady wave train. Experimental results and numerical results have similar divergence angles, although the intensity is different. It should be stated that the intensity of wave amplitude is dependent on wave steepness, and this is the case when the wave steepness is higher than the case of Fig. 22. Therefore, the amplitude intensity is larger than the case of Fig. 21 and computational results. Particularly, such trend is clearly shown in Fig. 23 which compares the overall-range measurement and numerical results for different advancing speeds.

Similar validation sets can be observed for the S-LNGC hull form, as shown in Figs. 24 and 25. Overall trends like the wave divergence angle or position of the peak amplitude are similar between measurement and computation results, and the phase and magnitude of unsteady waves are similar. However, experimental results show larger intensity than linear results, which may arise because linear solution in this study does not consider the wake, breaking waves, viscosity, or nonlinear hull form effects. For the S-LNGC hull, the bow flares, which is related to plunging wave breaking. The wave pattern differs near the position of the overturning wave at the bow shoulder. This may lead to differences between linear calculation and model measurement, even in steady calm water and linear wave conditions.

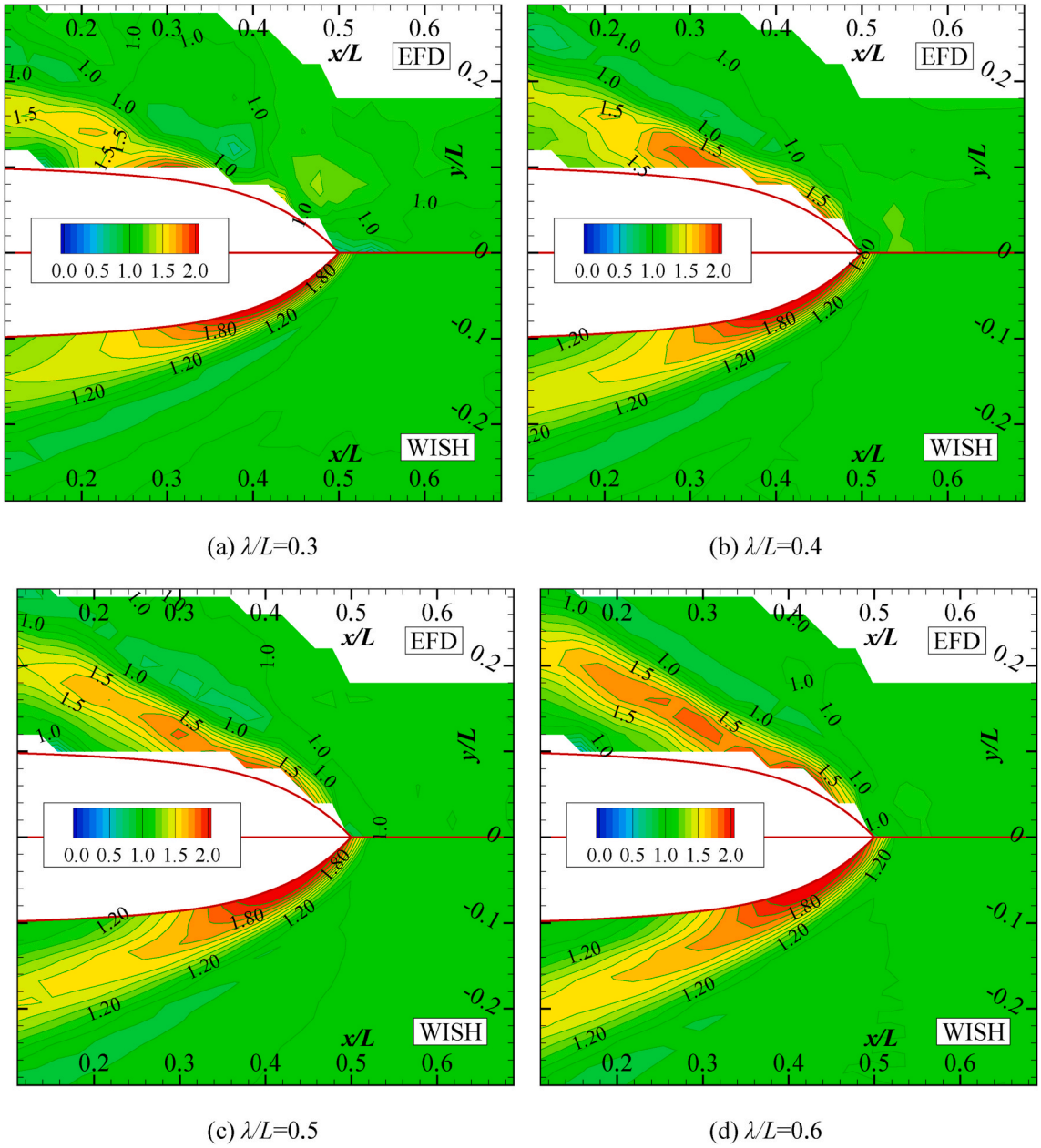

(a) λ/L=0.3 (b) λ/L=0.4

(c) λ/L=0.5 (d) λ/L=0.6

Fig. 22. Comparison of the first harmonic amplitude (ζ_1/A): experiment vs. linear computation, blunt Wigley hull, Fn = 0.2, λ/L = 0.3–0.6, H/λ = 1/40 in experiment.(a) λ/L = 0.3 (b) λ/L = 0.4.

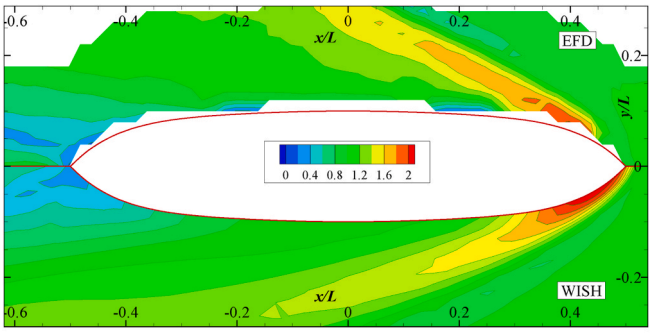

(a) Fn=0.15

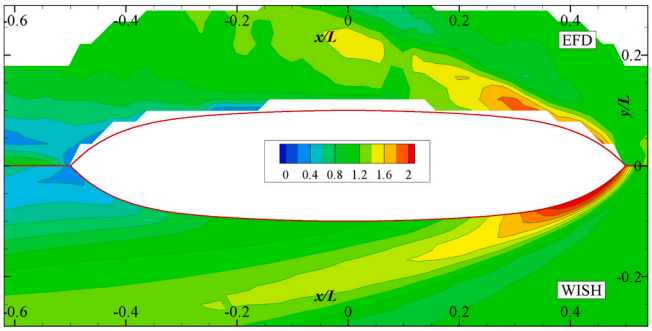

(b) Fn=0.20

Fig. 23. Comparison of the first harmonic amplitude (ζ_1/A) in overall range: experiment vs. linear computation, blunt Wigley hull, $Fn = 0.15$, 0.2, $\lambda/L = 0.4$, $H/\lambda = 1/40$ in experiment.(a) $Fn = 0.15$(b) $Fn = 0.20$.

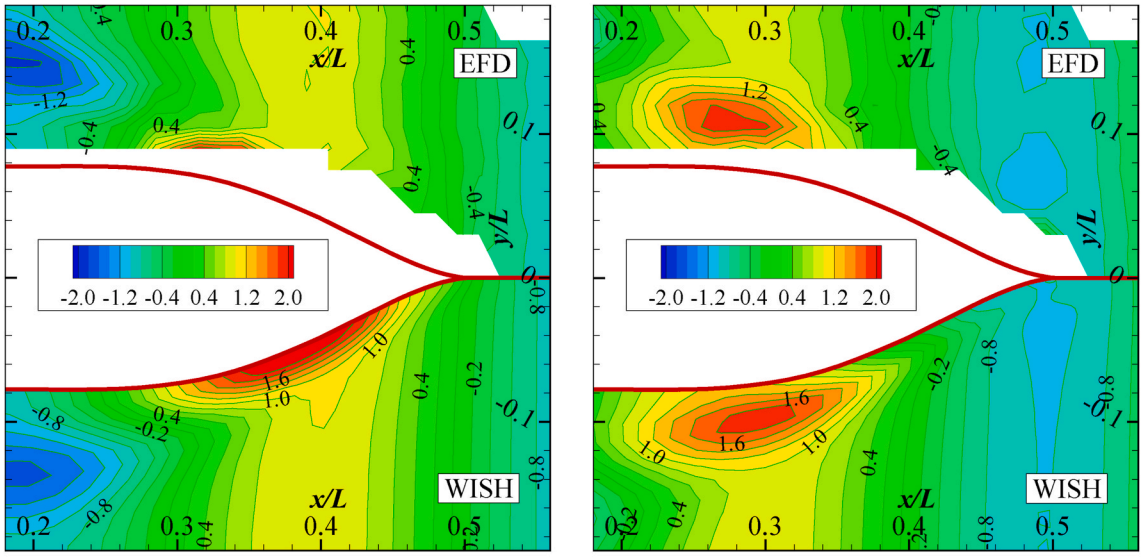

(a) $t=t_1+T_e/4$ (b) $t = t_1+T_e/2$

Fig. 24. Comparison of the first harmonic component of instantaneous wave elevation ($\zeta_1(t)/A$): experiment vs. linear computation, S-LNGC, $Fn = 0.188$, $\lambda/L = 0.4$, $H/\lambda = 1/80$ in experiment, T_e: encounter wave period.(a) $t=t_1+T_e/4$ (b) $t = t_1+T_e/2$..

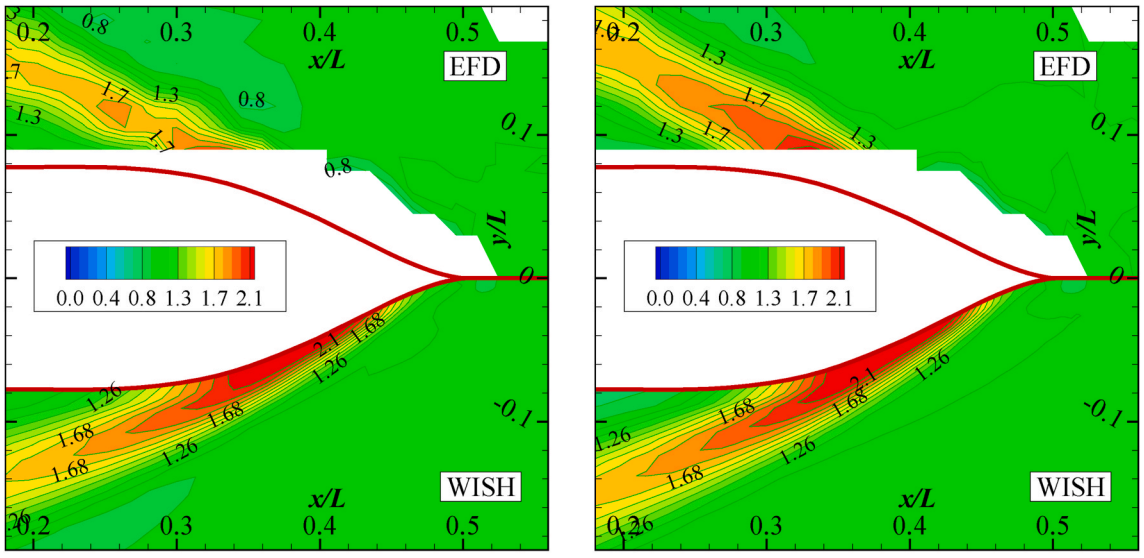

Fig. 25. Comparison of the first harmonic amplitude (ζ_1/A): experiment vs. linear computation, S-LNGC, $Fn = 0.188$, $\lambda/L = 0.4$–0.5, $H/\lambda = 1/40$ in experiment.(a) $\lambda/L = 0.4$ (b) $\lambda/L = 0.5$.

7. Conclusions

In this study, steady and unsteady wave elevations were measured around two hull forms in head sea condition. The mean, linear and second-order components of wave elevation were compared for different wave steepness, speed, and hull forms. Based on this research, the following conclusions are made:

- Data sets for unsteady wave components are obtained for a mathematical hull and a practical ship hull. The instantaneous local and global free surface elevations were collected around the ships under free vertical motion in head waves, and these data can be good reference data for benchmark test or validation data of numerical computation.
- Repeat tests showed the reliability of the present analysis scheme. To achieve better accuracy of elevation measurement, careful measurement and outlier analysis are needed particularly when the wave steepness becomes high. Moreover, it should be aware that the wave signals measured near the model hull and near the wave maker may have some difference, resulting in different normalized quantities of wave elevation. Such difference may be increased when the nonlinearity of incident waves and/or bow waves are stronger and wave length is short. It is obvious that uncertainty of measurement is sensitive to the accuracy of wave amplitude particularly in short waves. This issue must be carefully studied in the future.
- In the observation on the mean and harmonic components of the disturbed wave elevation around the ship hulls, the nonlinearity is clear around the ship bow and stern where large pressure variation occurs. Although the linear component is dominant, the nonlinear components are not ignorable and the degree of nonlinearity differs for each condition. Differences can be found related to wave breaking and the resultant disturbed wave for various advancing speeds.
- The comparison of wave elevation and component between numerical computation and experimental measurement shows fair agreement. The computational results based on linear potential theory and Rankine panel method show very similar wave component and bow wave angle although the intensity of wave amplitude are slightly different. This can justify the applicability of linear potential theory in seakeeping analysis even though it does not consider the ship wake, wave breaking, or nonlinear components.

CRediT authorship contribution statement

Jaehoon Lee: Investigation, experiment, computation, Formal analysis. **Yonghwan Kim:** Supervision, Formal analysis, Methodology.

Declaration of competing interest

The authors declare that they have no known competing financial interests or personal relationships that could have appeared to influence the work reported in this paper.

Acknowledgement

This study was carried out under the supports of the Lloyd's Register Foundation (LRF)-Funded Research Center(LRFC) at Seoul National University. Their support is greatly appreciated. In addition, the administrative supports of the Research Institute of Marine System Engineering (RIMSE) and the Institute of Engineering Research(IOER) at Seoul National University are appreciated.

References

Benjamin, T.B., Feir, J.E., 1967. The disintegration of wave trains on deep water Part 1. Theory. J. Fluid Mech. 27 (3), 417–430.
Faltinsen, O.M., 1990. Sea Loads on Ships and Offshore Structures. Cambridge University Press.
Gui, L., Longo, J., Metcalf, B., Shao, J., Stern, F., 2001. Forces, moment, and wave pattern for surface combatant in regular head waves Part I. Measurement systems and uncertainty assessment. Exp. Fluid 31 (6), 674–680.
Gui, L., Longo, J., Metcalf, B., Shao, J., Stern, F., 2002. Forces, moment and wave pattern for surface combatant in regular head waves Part II. Measurement results and discussions. Exp. Fluid 32 (1), 27–36.
ITTC, 2014. Prediction of Power Increase in Irregular Waves from Model Test(7.5-02-07-02.2). ITTC Recommended Procedures and Guidelines.
ITTC, 2017a. Analysis Procedure for Model Tests in Regular Waves(7.5– 02–07–03.2. ITTC Recommended Procedures and Guidelines.
ITTC, 2017b. Seakeeping Experiments(7.5–02–07–02.1). ITTC Recommended Procedures and Guidelines.
Iwashita, H., Ohkusu, M., 1990. Hydrodynamic forces on a ship moving at forward speed in waves. Naval Architect. Ocean Eng. 28, 87–109.

Iwashita, H., Elangovan, M., Kashiwagi, M., Sasakawa, T., 2011. On unsteady wave pattern analysis of ships advancing in waves. J. Jpn. Soc. Nav. Archit. Ocean Eng. 13, 95–106.
Janson, C.E., Spinney, D., 2004. A comparison of four wave cut analysis methods for wave resistance prediction. Ship Technol. Res. 51 (4), 173–184.
Kashiwagi, M., 2013. Hydrodynamic study on added resistance using unsteady wave analysis. J. Ship Res. 57 (4), 220–240.
Kim, K.H., Kim, Y., 2009. Numerical analysis of added resistance on ships by a time-domain rankine panel method. In: Proceedings of the Society of Naval Architects of Korea, pp. 29–30. Mungyeong, Korea.
Kim, K.H., Kim, Y., 2011. Numerical study on added resistance of ships by using a time-domain Rankine panel method. Ocean Eng. 38 (13), 1357–1367.
Kim, T.Y., Yoo, S., Oh, S., Kim, H.J., Lee, D., Kim, B., 2017. Numerical and experimental study on the estimation of added resistance of an LNG carrier in waves. In: Proceedings of the Twenty-Seventh International Ocean and Polar Engineering Conference, pp. 25–30. San Francisco, CA, USA.
Kim, W.J., Van, S.H., Kim, D.H., 2001. Measurement of flows around modern commercial ship models. Exp. Fluid 31 (5), 567–578.
Kim, Y., Park, D.M., Lee, J.H., Lee, J., Kim, B.S., Yang, K.K., Oh, S., Lee, D.Y., 2019. Numerical analysis and experimental validation of added resistance on ship in waves. J. Ship Res. 63 (4), 268–282.
Kompe, A., 2014. Implementation and validation of a wave cut analysis method for the wave resistance prediction from potential flow. Master thesis, TUHH.
Lake, B.M., Yuen, H.C., Rungaldier, H., Ferguson, W.E., 1977. Nonlinear deep-water waves: theory and experiment. Part 2. Evolution of a continuous wave train. J. Fluid Mech. 83 (1), 49–74.
Lee, J., Kim, Y., Choi, J.E., Kim, C.H., Lee, Y.B., 2018. Towing-tank experiment and analysis of nonlinear roll damping for a drillship with different appendages. Ocean Eng. 160, 324–334.
Lee, J., Park, D.M., Kim, Y., 2017. Experimental investigation on the added resistance of modified KVLCC2 hull forms with different bow shapes. Proc. IME M J. Eng. Marit. Environ. 231 (2), 395–410.
Lee, J.H., Kim, B.S., Kim, Y., 2017. Effects of analysis method for ship steady flows in numerical analysis of added resistance in waves. Pusan, Korea. In: Proceedings of the Society of Naval Architects of Korea, pp. 19–20 (April).
Lugni, C., Landrini, M., Ohkusu, M., La Gala, F., 2013. Experimental study of the diffracted wave pattern around a fast displacement vessel. In: Proceeding of the 18th Int. Workshop on Water Waves and Floating Bodies. LeCroisic, France.
Maury, C., Delhommeau, G., Boin, J.P., Guilbaud, M., 2003. Comparison between numerical computations and experiments for seakeeping on ship models with forward speed. J. Ship Res. 47 (4), 347–364.
Olivieri, A., Pistani, F., Wilson, R., Campana, E.F., Stern, F., 2007. Scars and vortices induced by ship bow and shoulder wave breaking. J. Fluid Eng. 129 (11), 1445–1459.
Park, D.M., Lee, J., Kim, Y., 2015. Uncertainty analysis for added resistance experiment of KVLCC2 ship. Ocean Eng. 95, 143–156.
Shigeru, N., et al., 1998. Image measurement of the wave height distributions around a ship hull in regular wave. J. Jpn. Soc. Naval Architects 184, 95–102 (Japanese).
Wehausen, J.V., 1973. The wave resistance of ships. Adv. Appl. Mech. 13, 93–245.
Yang, K.K., Kashiwagi, M., Kim, Y., 2020. Numerical study on ship-generated unsteady waves based on a Cartesian-grid method. J. Hydrodyn. 1–15.